arXiv:1211.1674v1 [astro-ph.CO] 7 Nov 2012

XMM-Newton Observations of Three Interacting Luminous Infrared Galaxies

Dale Mudd[1], Smita Mathur[1,2], Matteo Guainazzi[3], Enrico Piconcelli[3], Stefano Bianchi[4], Stefanie Komossa[5], Cristian Vignali[6], Giorgio Lanzuisi[7], Fabrizio Nicastro[8,9], Fabrizio Fiore[10], Roberto Maiolino[11,12]

`mudd@astronomy.ohio-state.edu`

November 9, 2012

ABSTRACT

We investigate the X-ray properties of three interacting luminous infrared galaxy systems. In one of these systems, IRAS 18329+5950, we resolve two separate sources. A second, IRAS 20550+1656, and third, IRAS 19354+4559, have only a single X-ray source detected. We compare the observed emission to PSF profiles and determine that three are extended in emission. One is compact, which is suggestive of an AGN, although all of our profiles have large uncertainties. We then model the spectra to determine soft (0.5–2 keV) and hard (2–10 keV) luminosities for the resolved sources and then compare these to relationships found in the literature between infrared and X-ray luminosities for starburst galaxies. We obtain luminosities of $\log(L_{\rm soft}/{\rm L}_\odot) = 7.32, 7.06, 7.68$ and $\log(L_{\rm hard}/{\rm L}_\odot) = 7.33, 7.07, 7.88$ for IRAS 18329+5950, IRAS 19354+4559, and IRAS 20550+1656, respectively. These are intermediate to two separate predictions in the literature for star-formation-dominated sources. Our highest quality spectrum of IRAS 20550+1656 suggests super-solar abundance of alpha elements at 2σ significance, with $\log\left(\frac{\alpha}{\alpha_\odot}\right) = [\alpha] = 0.4 \pm 0.2$. This is suggestive of recent enrichment with Type II supernovae, consistent with a starburst environment. The X-ray properties of the target galaxies are most likely due to starbursts, but we cannot conclusively rule out AGN.

---

[1] Department of Astronomy, The Ohio State University, Columbus, Ohio 43210, USA

[2] Center for Cosmology and Astro-Particle Physics, The Ohio State University, Columbus, OH 43210

[3] European Space Astronomy Centre of ESA, PO Box 78, Villanueva de la Cañada, 28691 Madrid, Spain

[4] Dipartimento di Fisica, Università degli Studi Roma Tre, via della Vasca Navale 84, 00416 Roma, Italy

[5] Max-Planck Institut für Radioastronomie, Auf dem Hügel 69, D-53121 Bonn, Germany

[6] INAF – Osservatorio Astronomico di Bologna, Via Ranzani 1, 40127 Bologna, Italy

[7] INAF – Istituto di Astrofisica Spaziale e Fisica Cosmica di Bologna, via Gobetti 101, 40129 Bologna, Italy

[8] Osservatorio Astronomico di Roma - INAF, Via di Frascati 33, 00040, Monte Porzio Catone, RM, Italy

[9] Harvard-Smithsonian Center for Astrophysics, 60 Garden St., MS-04, Cambridge, MA 02138, USA

[10] INAF – Osservatorio Astronomico di Roma, Via di Frascati 33, 00040 Monteporzio Catone, Italy

[11] Department of Physics, University of Cambridge, 19 JJ Thomson Avenue, Cambridge, CB3 0HE, United Kingdom

[12] Kavli Institute for Cosmology, Madingley Road, Cambridge, CB3 0HA, United Kingdom

Subject headings: galaxies: active, galaxies: interactions, galaxies: nuclei, galaxies: starburst, X-rays, infrared radiation

1. Introduction

Over the past few decades, much work has emphasized the role and importance of mergers in shaping galactic evolution (Toomre & Toomre 1972; Ellison et al. 2011; Hopkins et al. 2006). In particular, mergers have been suggested as potential drivers of starbursts and AGN activity (Bauer et al. 2004; Summers et al. 2004; Bell et al. 2011; Komossa et al. 2003; Teng et al. 2009; Piconcelli et al. 2010). Broadly, the hierarchical growth simulations in Hopkins et al. (2006) paint a picture in which galactic mergers provide gas inflows to ignite starbursts, which are then followed by growth of the central supermassive black holes (SMBHs) of galaxies, sometimes leading to the birth of an AGN until feedback possibly stops the process. The interactions of two galaxies can also cause both of their central SMBHs to become active simultaneously, resulting in a dual AGN (Komossa 2006). A complication in this scenario is that some simulations suggest that most of the dual AGN activity is non-simultaneous, particularly during their highest luminosity phases when they would also be easiest to detect (Van Wassenhove et al. 2012). Other simulations have suggested that this merger scenario was more important in the past, when interacting systems were much more gas-rich, but that it still plays a role in the local universe for lower-luminosity AGN (Draper & Ballantyne 2012).

Luminous infrared galaxies (LIRGs), galaxies that have infrared luminosities $L_{IR} \geq 10^{11}$ $L_{\odot}$ (for a review, see Sanders & Mirabel 1996 and references therein), where IR ranges here span 8-1000 μm, are often found to be mergers and have distinctive morphologies (Yuan et al. 2010). The emission from such systems is prominent in the infrared (IR) portion of the spectrum due to heavy dust reprocessing. The Great Observatory All-sky LIRG Survey (GOALS), which is observing LIRGs across the electromagnetic spectrum (e.g. Armus et al. 2009 and Iwasawa et al. 2011), and other studies (e.g. Ptak et al. 2003; Braito et al. 2009; Alonso-Herrero et al. 2011; Charmandaris et al. 2010) have attempted to determine if the drivers of the high IR luminosities in these systems are central starbursts or AGN. In one such system, NGC 6240, two separate AGN from merging galaxies, were detected by Komossa et al. (2003). This discovery has fueled much discussion about the nature of dual AGN, their prevalence, and lifetimes.

Several studies have investigated the connection between AGN activity and environment. When looking at quasars, Serber et al. (2006) found a local overdensity of $\sim$3 around the brightest objects and an overdensity of $\sim$1.4 for fainter quasars. They also found that the overdensity around quasars relative to L* galaxies is about unity at 1 Mpc, but increases at smaller scales. Ellison et al. (2011) reported a similar result focusing on AGN; they found AGN are 2.5 times more likely to be in pairs than similar but inactive galaxies. Using the Swift's Burst Alert Telescope (BAT) AGN sample, Koss et al. (2011) also found evidence that AGN activity is associated with mergers and interactions. Specifically, they report that 24% of BAT AGN are undergoing a merger, whereas this number is closer to 1% for a sample of normal galaxies. These works and work done by other authors (e.g., Ajello et al. 2012) suggest that a galaxy's environment can play a non-negligible role in fueling AGN, whether through interactions or mergers with nearby galaxies.

Because of heavy obscuration at most wavelengths in these dust-enshrouded systems, X-rays, which are less attenuated, become a useful tool to probe behind optically thick screens. The hard X-ray band (2–10 keV) luminosity of AGN is typically described by a power law with photon index $\Gamma \sim 2$. A proposed explanation for this spectral behavior is that an accretion disk feeding the central SMBH thermally emits in the optical and UV. These photons inverse Compton upscatter to X-rays off of a hot plasma surrounding the disk (Shapiro et al. 1976; Sunyaev & Titarchuk 1980; Haardt & Maraschi 1993). Much of a galaxy's SMBH growth is believed to occur in regions heavily obscured by dust (Hopkins et al. 2006; Fabian 1999), so searching in X-rays is one of the few viable options for spotting this phase, provided the column density is not overly large ($\gtrsim 10^{24}\,\mathrm{cm}^{-2}$).

AGN activity is not the only interesting phenomenon strongly associated with galactic interactions. Another prominent event often triggered is a marked increase in the star formation rate of one or both component galaxies, provided neither is gas poor. If this increase is large enough, the galaxy becomes a starburst. Muzzin et al. (2012) suggest that, while the gross properties of star-forming galaxies are tied to their stellar masses, their environment appears to regulate the fraction of systems that are starbursting.

Like AGN, star-forming regions also produce specific X-ray signatures (e.g., Georgakakis et al. 2011). The ionizing photons from supernovae and short-lived O and B stars form a thermal plasma typically between 0.1-1 keV. A secondary power law component, associated with high mass X-ray binaries (HMXBs), indicative of recent star formation (Fabbiano 2006), is often observed in starburst systems. These are said to trace recent or ongoing star formation because they require an OB star around a neutron star (NS) or black hole (BH) and thus only have a lifetime of 10^{6-7} years. HMXBs have been observed with a range of photon indices, typically lying within 1-1.5, while low mass X-ray binaries (LMXBs), a possible contaminant, are usually described by either a power law with index $\sim$1.6 or bremsstrahlung at 7.3 keV (Fabbiano 2006; Persic & Rephaeli 2003). These spectral indices can run as steep as 2-3 in some cases. LMXBs do not trace recent star formation, however, since they are associated with lower mass companions around a NS or BH and thus have lifetimes that are 100–1000 times longer.

Kennicutt (1998) associated star forming regions with IR emission due to dust reprocessing. Ranalli et al. (2003), hereafter R03, proposed an X-ray/IR luminosity relationship in IR-bright galaxies, arguing that star formation is traced in the IR from reprocessing and in X-rays from HMXBs, provided there is no AGN present. The use of X-rays as a tracer of star formation also requires that LMXBs are a negligible contributor, which is generally a safe assumption for the high star formation rates encountered in starbursting systems. One can then use these relations to predict the X-ray output of a system originating from star formation alone. It should be noted, however, that the existence of either a starburst or an AGN does not discount the other (Sani et al. 2010; Santini et al. 2012). Additionally, some argue for a more complete picture taking into account escaping, non-reprocessed UV radiation when attempting to synthesize star formation data (e.g, Vattakunnel et al. 2011).

In this paper we attempt to use the association between AGN activity, starbursts, mergers, and, by extension, large IR luminosity, to search for dual AGN. We also study the X-ray/IR relationships to better understand the current star formation rate due to interaction processes in LIRGs. In §2, we describe our sample selection and discuss the systems we examined in detail. §3 presents image and spectral analysis as well as the luminosities we obtain. §4 compares our data to existing IR/X-ray relations and discusses our prospectives on dual AGN detection. Finally, we conclude in §5.

We adopt a cosmology of H_0 = 70 km s^{-1} Mpc^{-1}, $\Omega_{\rm M}$ = 0.27, and Ω_Λ = 0.73.

2. Sample

We derived our sample from a subset of nearby IR bright galaxies presented in Arribas et al. (2004). Our systems were nearby (redshifts of $0.03 < z < 0.07$) to ensure a higher number of photon counts and were known to be interacting with two optical nuclear regions, though there was some uncertainty about the location of the secondary nucleus in IRAS 20550+1656. All were LIRGs, and many had roughly measured nuclear separations. We selected based on interaction class using the scheme proposed in Surace (1998) and refined in Veilleux et al. (2002), restricting our sample to class IIIa and IIIb systems with nuclear separations around 10 kpc. A class IIIa system is composed of two or more galaxies with evidence of tidal interactions (tails, bridges) and with nuclear separation of greater than 10 kpc, whereas a class IIIb system has similar tidal structures but with nuclear separation less than 10 kpc. Additionally, we required that systems have angular separations that would likely be resolvable with *XMM Newton*, or $\sim 8-10''$. After this, we selected the LIRGs with the highest IR fluxes, and, by association, likely the most X-ray counts barring the system being Compton thick. Three systems met our criteria: IRAS 18329+5950, IRAS 19354+4559, and IRAS 20550+1656. We observed these with *XMM Newton* and restricted all analyses to 0.3–10 keV so as to stay in range of the detector's optimal sensitivity.

Our observations are summarized in Table 1.

2.1. IRAS 18329+5950

IRAS 18329+5950 is a class IIIa system composed of two merging galaxies with estimated nuclear separations of $28''$ (Arribas et al. 2004). The offset in declination ($5\farcs70$) of the two galaxies in this system is much smaller than the offset in right ascension ($27\farcs5$). In projection, it appears that the nucleus of the eastern component (18329E) is close to the plane of the disc of the western component (18329W). The system is classified as a LIRG in the IRAS Revised Bright Galaxy Sample (hereafter RBGS; Sanders et al. 2003). Using the RBGS fluxes, we calculate luminosities of $\log(L_{\rm FIR}/{\rm L}_\odot)$ = 11.48 (where FIR denotes 40-400μm) and $\log(L_{\rm IR}/{\rm L}_\odot)$ = 11.60 based on the redshift of z=0.029, which corresponds to a distance of $\sim$128.5 Mpc (Armus et al. 2009). Optical line ratios, more extensively discussed in §4.5, suggest that this system is a starburst or starburst/AGN composite.

2.2. IRAS 19354+4559

IRAS 19354+4559 is a class IIIb merger system with nuclear separations of approximately $8\overset{\prime\prime}{.}5$ (Arribas et al. 2004). In this case, the offsets in right ascension and declination are comparable, being $6\overset{\prime\prime}{.}7$ and $5\overset{\prime\prime}{.}3$, respectively. Both galaxies have significant tidal features suggestive of mutual interaction and appear as edge-on disks, although the eastern component has several foreground stars contaminating the optical images, partially confusing the orientation. Using fluxes from the RBGS, we calculate a FIR luminosity $\log(L_{\rm FIR}/{\rm L}_{\odot}) = 11.06$ and an upper limit IR luminosity of $\log(L_{\rm IR}/{\rm L}_{\odot}) = 11.85$ based on the redshift of z=0.067, which corresponds to a distance of $\sim$289 Mpc (Lawrence et al. 1999). We did not find any IR or optical line diagnostics for this system.

2.3. IRAS 20550+1656

Similarly, IRAS 20550+1656 is a class IIIb merger system. The separation between the optical nuclei is uncertain, but believed to be about $11\overset{\prime\prime}{.}7$ (Arribas et al. 2004). From the RBGS fluxes, we calculate luminosities of $\log(L_{\rm FIR}/{\rm L}_{\odot}) = 11.66$ and $\log(L_{\rm IR}/{\rm L}_{\odot}) = 11.94$ for a redshift of z=0.036, corresponding to a distance of $\sim$161 Mpc (Armus et al. 2009). Optical (Baan et al. 1998) and IR (Inami et al. 2010) spectroscopy and line ratio diagnostics indicate that this system is a starburst. The Spitzer data in particular (Inami et al. 2010) suggests that 80% of the IR luminosity comes from a region outside the nuclei of the two interacting galaxies in this merger.

3. *XMM-Newton* Observations

3.1. Image Analysis

All data were taken with the *EPIC* instruments on board *XMM Newton* and reduced using XMM SAS Version 12.0.1. As is typical in X-ray image analysis, we filtered the event files to discard any time interval

Table 1. Observational Data

IRAS Name	Observation ID	Date	Exposure (ks)	Distance (Mpc)	Separation	Separation (kpc)	HR	Source Counts
18329+5950E	0670140301	2011-05-04	9.4	128.5	$28''$	17.4	-0.52 ± 0.20	170
18329+5950W	0670140301	2011-05-04	9.4	128.5	$28''$	17.4	-0.49 ± 0.18	173
19354+4559	0670140501	2011-05-10	13.2	289	$8\overset{\prime\prime}{.}5$	11.91	-0.36 ± 0.30	53
20550+1656	0670140101	2011-10-28	58.2	161	$11\overset{\prime\prime}{.}7$	9.13	-0.52 ± 0.04	2900

Note. — Separation refers to the projected nuclear separation between the interacting galaxies; the first is angular separation while the second is physical separation. HR is the hardness ratio. Note that exposure times are after applying filtering for cosmic rays.

with an abrupt spike in counts above the base threshold in order to minimize contamination from cosmic rays and other short, time-variant noise sources. As the *EPIC MOS* cameras have a smaller pixel scale than the *EPIC PN* by nearly a factor of four, we first tried creating images and radial profiles using this data. Unfortunately, there were not enough counts in the *MOS* images to determine the radial profiles. There were more counts in the *PN* detector, however, so we proceeded to use this set for our analysis. Processed *EPIC PN* images for the three sources in our sample are shown in Figure 1. The total exposure time for IRAS 18329+5950 was 37.2 ks, with 9.4 ks usable after background filtering. The left panel of Figure 1 demonstrates that the nuclear regions of the two separate galaxies in IRAS 18329+5950 are resolved in X-rays. The two spectra were extracted from a region of radius $13''$ centered around α = 18:33:37.67, δ = +59:53:23.52 for 18329E and α = 18:33:33.87, δ = +59:53:14.85 for 18329W. The background was selected from a region of the same size in a nearby location on the same CCD in order to minimize contamination from inter-chip variance. Additionally, the middle and right panels of Figure 1 show that for both IRAS 19354+4559 and IRAS 20550+1656 the nuclei from the individual component galaxies were not distinctly separable. Thus only a single spectrum could be extracted and examined for each of these sources. We analyzed a region of radius $11''$ centered on α = 19:36:56.13, δ = +46:06:26.24 with a final exposure time of 13.2 ks for IRAS 19354+4559. The total exposure time pre-filtering was 33 ks. For IRAS 20550+1656, we extracted a region of radius $19''$ centered on α = 20:57:24.09, δ = +17:07:38.94 with an initial exposure duration of 77 ks and final time of 58.2 ks.

As hinted at above, one avenue for discerning the probable X-ray source type is to compare the radial profile of the observed flux to the PSF of the detector. A lone AGN, being a point-like source, would have a profile that approximately matched the PSF's, whereas a starburst or a blend of starburst with an AGN would be more extended. We used the *XMMSAS* task *eradial* to calculate the sources' radial profile distributions at an energy of 2-8 keV. We chose this energy range because if an AGN is indeed present and is not heavily obscured, it would likely provide a greater fractional contribution to the hard band flux than the soft band as compared to a starburst region. The *eradial* task modeled the PSF at 5 keV, the midpoint of our hard energy range, using the built-in ELLBETA model type. This model is based around an elliptical King profile, with an added Gaussian to account for spokes. As the PSFs have an arbitrary normalization, we renormalized all

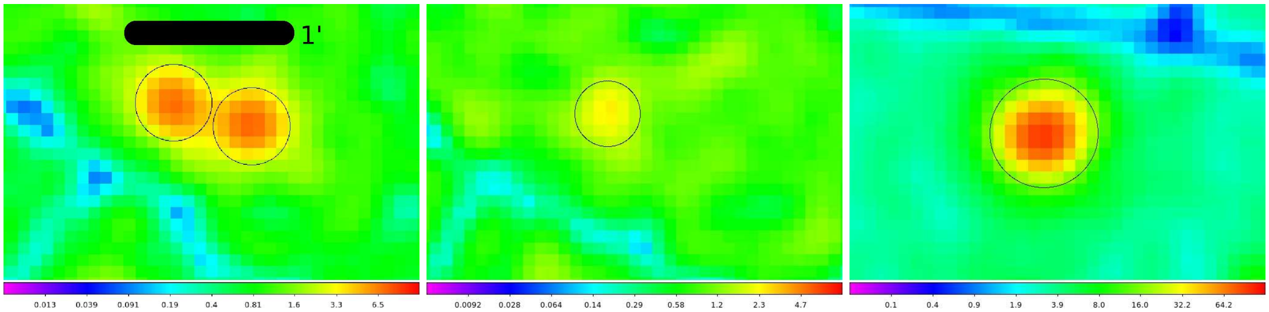

Fig. 1.— Smoothed, false-color *XMM Newton* images of the three objects in our sample with the spectral extraction region, described in §3, overplotted as black circles. All images are scaled logarithmically over the range 0.5-10keV. *Left*: IRAS 18329+5950 *Middle*: IRAS 19354+4559 *Right*: IRAS 20550+1656.

of the counts per square arcsecond of the background-subtracted data to the peak surface brightness of its corresponding object so as to provide an easier comparison to the source. These results are shown in Figure 2. Our systems appear to be at least marginally extended with respect to the PSF over our energy range, if not greatly extended. The exception is 18329E, which is fairly consistent with being point-like.

3.2. Spectral Analysis

Following extraction, we performed spectral analysis using XSPEC v12.7.0. We modeled each system with multiple components in combination to account for AGN, possibly obscured, and starbursts in an attempt to recover the observed count and energy distributions. We were, however, limited in the complexity of our models due to low source number counts, as can be seen in Table 1. Our fewest counts came from IRAS 19354+4559 with 53. Both sources in IRAS 18329+5950 had around 200 counts, and IRAS 20550+1656 had over an order of magnitude greater at 2900.

For IRAS 18329+5950, due to the low number counts in both sources, we decided not to bin the data and used Cash statistics rather than fit based on the more commonly used reduced χ^2value (Cash 1979). We took into account the Galactic absorption, with hydrogen column density along this line of sight of $N_H^{\rm Gal} = 4.48 \times 10^{20}\,{\rm cm}^{-2}$ (Dickey & Lockman 1990), using the “tbabs” model (Wilms et al. 2000). 18329E was best fit by a power law component of spectral index $\Gamma = 1.5 \pm 0.5$ and an additional MEKAL plasma (Mewe et al. 1985, 1986; Liedahl et al. 1995) of temperature $0.65^{+0.19}_{-0.17}$ keV to account for the soft excess shown in Figure 3. The final model had $C = 94.78$ for 115 degrees of freedom. The overall Galactic-absorption-corrected X-ray (0.5-10 keV) luminosity of the galaxy using this model is found to be $L_{\rm X} = 7.6^{+3.7}_{-2.2} \times 10^{40}$ erg s^{-1}. From Table 2, we note that this source is dominated in the hard band by the power law component, and most likely dominated by the plasma in the soft band, although the two are roughly equivalent in this energy range. There is a clear soft excess component around 0.5 keV. We try to recover this with a stronger plasma and a steeper power law, but the fits do not converge in this scenario.

The system 18329W, modeled in Figure 4, was also best fit by a Galactic absorbed power law and MEKAL plasma with $C = 92.31$ for 116 degrees of freedom. Here, the spectral index was $\Gamma = 1.6^{+0.4}_{-0.5}$ and the temperature of the plasma was $0.69^{+0.25}_{-0.18}$ keV. It should be noted that both of these models were fixed at solar metallicity via the prescription in Anders & Grevesse (1989), which is used by default in XSPEC. Like with 18329E, Table 2 indicates that 18329W derives most of its model’s hard band luminosity from the power law and comparable amounts from both the plasma and power law in the soft band, with a total Galactic-absorption-corrected X-ray luminosity of $L_{\rm X} = 8.7^{+2.0}_{-4.0} \times 10^{40}$ erg s^{-1}.

With fewer than a third the counts of either source in IRAS 18329+5950, the data for IRAS 19354+4559 were also fit without binning and using Cash statistics rather than reduced χ^2. Even so, multicomponent models were not well-constrained due to the paucity of counts. As such, we tried modeling the system with a plasma, black body, and power law component separately, each with Galactic absorption. The best fit, seen in Figure 5, (with $C = 36.13$ for 45 degrees of freedom) is the power law, with a spectral index of $2.4^{+1.1}_{-0.9}$. After accounting for Galactic absorption through a column density $N_H^{\rm Gal} = 1.2 \times 10^{21}$ cm^{-2} (Dickey & Lockman

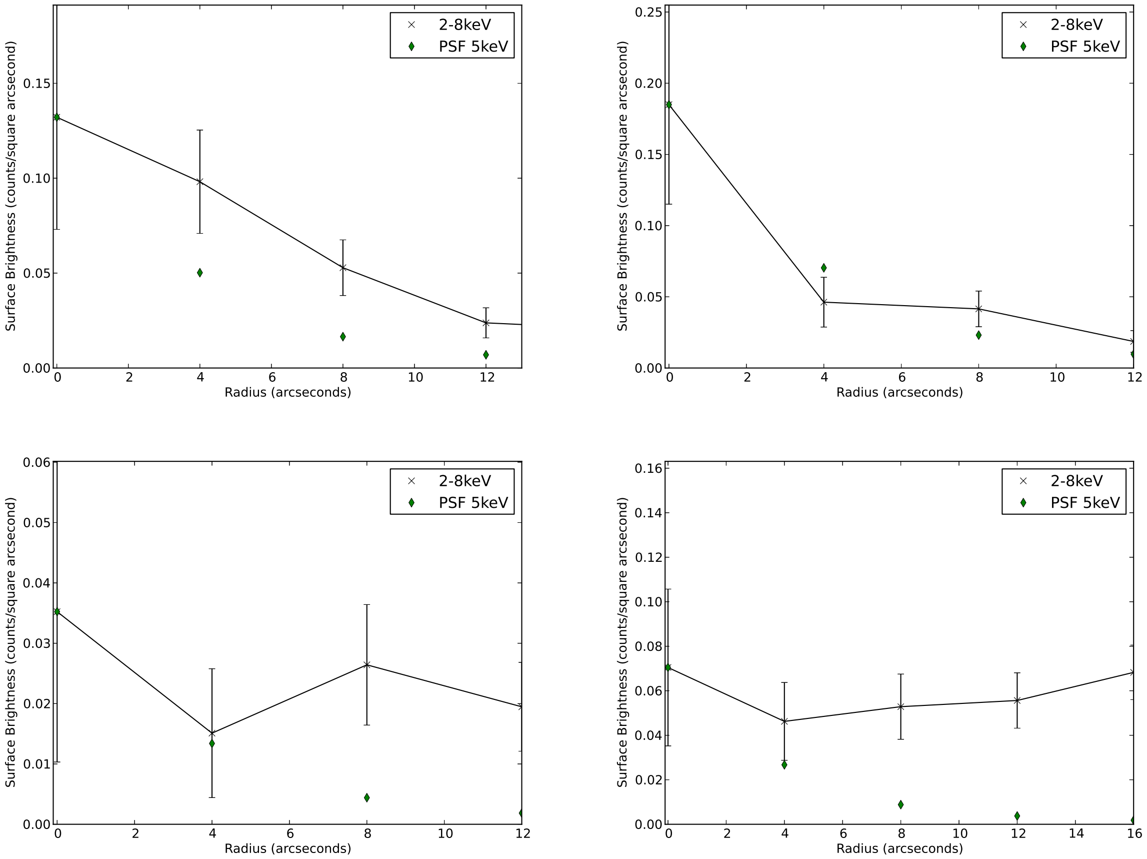

Fig. 2.— Radial profile plots for the three sources at 2-8 keV as well as the models of the detector's PSF at 5keV at the same locations. *Top*: IRAS 18329+5950 West (18329W, *left*) and IRAS 18329+5950 East (18329E, *right*). *Bottom*: IRAS 19354+4559 (*left*) and IRAS 20550+1656 (*right*).

Table 2. Model Component Luminosities

IRAS Name	Component	$L_{\rm soft}$ $\log(L_{\rm band}/{\rm L}_\odot)$	$L_{\rm hard}$ $\log(L_{\rm band}/{\rm L}_\odot)$	$L_{\rm soft\,+\,hard}$ $\log(L_{\rm band}/{\rm L}_\odot)$
18329+5950E	Full Model	$7.01^{+0.17}_{-0.17}$	$6.98^{+0.18}_{-0.13}$	$7.30^{+0.17}_{-0.15}$
	Power Law	$6.60^{+0.18}_{-0.12}$	$6.97^{+0.18}_{-0.13}$	$7.13^{+0.18}_{-0.13}$
	MEKAL Plasma	$6.79^{+0.16}_{-0.20}$	$5.23^{+0.15}_{-0.20}$	$6.81^{+0.15}_{-0.20}$
18329+5950W	Full Model	$7.04^{+0.13}_{-0.28}$	$7.07^{+0.05}_{-0.25}$	$7.36^{+0.09}_{-0.27}$
	Power Law	$6.60^{+0.18}_{-0.12}$	$6.93^{+0.18}_{-0.12}$	$7.10^{+0.18}_{-0.12}$
	MEKAL Plasma	$6.73^{+0.21}_{-0.29}$	$5.25^{+0.20}_{-0.29}$	$6.75^{+0.20}_{-0.29}$
19354+4559	Power Law	$7.06^{+0.17}_{-0.24}$	$7.07^{+0.17}_{-0.24}$	$7.37^{+0.16}_{-0.24}$
20550+1656	Full Model	$7.68^{+0.05}_{-0.07}$	$7.88^{+0.07}_{-0.07}$	$8.09^{+0.06}_{-0.07}$
	Power Law	$7.38^{+0.07}_{-0.07}$	$7.88^{+0.06}_{-0.08}$	$8.00^{+0.06}_{-0.08}$
	MEKAL Plasma	$7.37^{+0.05}_{-0.07}$	$6.20^{+0.06}_{-0.06}$	$7.39^{+0.06}_{-0.06}$

Note. — Comparison of X-ray luminosities of various model components. Luminosities are reported in the form $\log(L_{\rm band}/{\rm L}_\odot)$. All models have been corrected for Galactic absorption. Also provided are the individual luminosities of each of the model components, except in the case of IRAS 19354+4559, which has only a single power law. Errors are calculated from the errors on the normalizations of each model component.

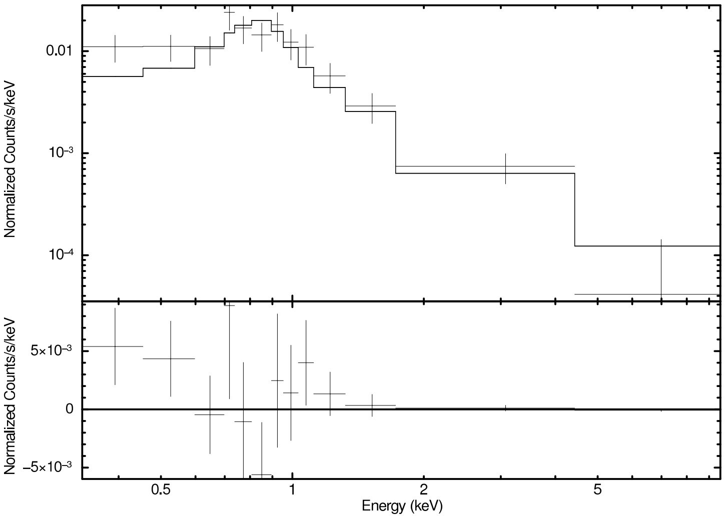

Fig. 3.— The best fit spectrum of the eastern source in IRAS 18329+5950 (18329E), composed of a power law of spectral index 1.5, a thermal plasma component with temperature 0.65 keV, and Galactic absorption taken from Dickey & Lockman (1990). The data is rebinned for illustration purposes. The bottom panel is the residuals between the fit and the data in units of counts per second.

1990), the combined soft (0.5–2 keV) and hard X-ray (2–10 keV) luminosity was $L_\mathrm{X} = 9.0^{+4.1}_{-3.8} \times 10^{40}$ erg s^{-1}. We then calculated the hardness ratio, HR, defined as

$$\mathrm{HR} \equiv \frac{H-S}{H+S}, \tag{1}$$

where H is the total counts in the hard band and S is the total counts in the soft band. For this system, we find the hardness ratio to be HR = -0.36 ± 0.30. While not conclusive, this negative hardness ratio suggests that the X-ray luminosity is most likely due to a starburst population or a heavily-obscured AGN (Fiore et al. 2000).

Finally, IRAS 20550+1656 was more complex to model due to the presence of bumps around 2 and 4-5 keV. Because of the larger number of counts, however, we were able to bin the raw spectrum such that each bin contained a minimum of 20 counts. The number of counts also permitted us to use reduced χ^2 fitting for this system. After being unable to fit the data well with any single component model, we tried several multicomponent models. We found the best fit consisted of Galactic absorption of a power law and plasma. Again, we corrected for the Galactic column density $N_H^{\mathrm{Gal}} = 1.10 \times 10^{21}$ cm^{-2} (Dickey & Lockman 1990). The spectral index of the best-fit power law was $\Gamma = 1.5^{+0.2}_{-0.1}$. The best-fit plasma temperature was 0.67 ± 4 keV. Universal solar abundances could reproduce most of the data, but were not able to explain the bump-like features. We then fit instead with a metal variant plasma, VMEKAL in XSPEC, to determine if any abundance patterns could match the observed spectrum. Testing each element individually, we found that the bump around 2 keV could be well-fit by super-solar silicon. We might expect to see enhanced levels of silicon from a starbursting region. This is because starbursts are a rich environment of massive stars, which become Type II supernovae and can pollute the region with alpha elements. To test this idea, we next fit the system with a model where all of the alpha elements were tied to the silicon value. This provided a better reduced χ^2, 0.8 for 109 degrees of freedom, than the solar metallicity plasma as well as the plasma with solely elevated silicon. It should be noted that we also fit with both alphas independent from one another as well as all metals as free parameters, but our data was unable to provide firm constraining power in either of these instances. The final fit, with the alphas fixed to the silicon value, has an abundance $\log\left(\frac{\mathrm{Si}}{\mathrm{Si}_\odot}\right) = [\mathrm{Si}] = 0.4 \pm 0.2$, and is shown in Figure 6.

We are still left with the prevalent bumps between 4-5 keV, as well as several smaller ones. If we fit the larger feature as a Gaussian emission line, the line has a central value of E = 4.3 ± 0.4 keV and line width of $\sigma = 0.4^{+0.5}_{-0.3}$ keV. If this feature is an emission line from the source, it is most likely Ca XX at 3.0185A, or $\sim$4.1 keV. We found no reports of this line in emission in the literature, though it may have been seen in absorption in a few systems (Tombesi et al. 2010). Due to the tenuous detection of this line and the marginal improvement to our fit after its addition, however, we report the model without this component as our best fit.

Overall, the observed luminosity of these conditions between both the soft and hard X-ray bands (0.5–10 keV) was $L_\mathrm{X} = 4.8^{+0.6}_{-0.8} \times 10^{41}$ erg s^{-1} after correcting for Galactic absorption. These parameters are summarized in Table 3. From Table 2, we note that this source is dominated in the hard band by the power law component, whereas the two components are comparable in the soft band, as with the other systems.

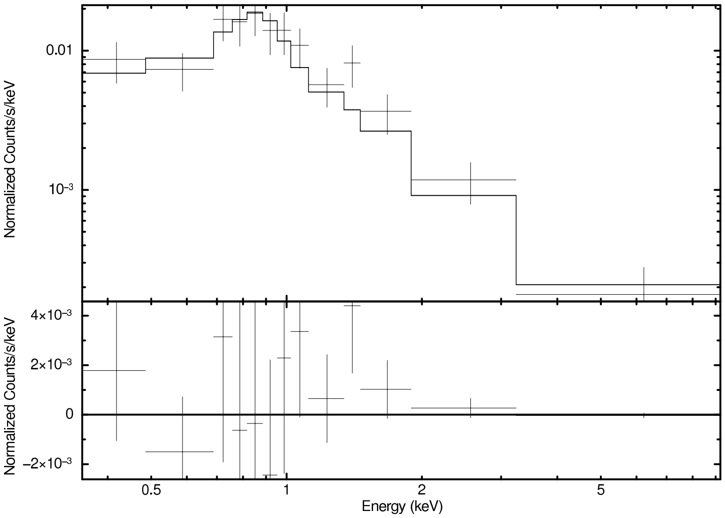

Fig. 4.— Similar to Figure 3, but for 18329+5950 (18329W). For this system, the power law index is 1.6 and MEKAL thermal plasma temperature is 0.69 keV.

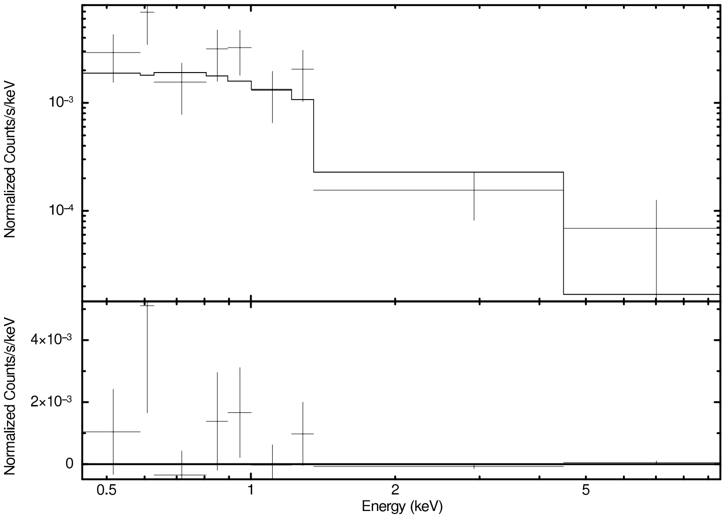

Fig. 5.— Similar to Figure 3 but for IRAS 19354+4559. Here the best fit model is comprised only of a power law, best fit by index 2.4, with Galactic absorption.

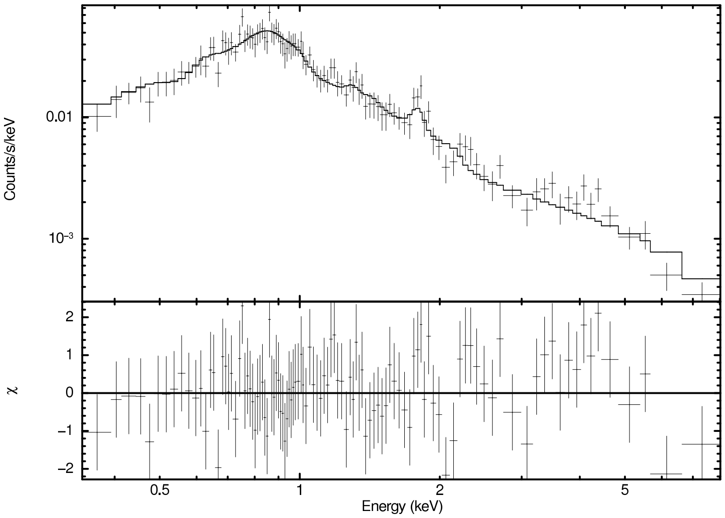

Fig. 6.— Similar to Figure 3 but for IRAS 20550+1656. The best-fit model here has a metal-variant MEKAL plasma of temperature *k*T ∼0.67 keV with the strong bump feature just below 2 keV in the spectrum fit by adopting a super-solar alpha abundance tied to silicon ($\log\left(\frac{\mathrm{Si}}{\mathrm{Si}_\odot}\right)$ = [Si] = 0.4). The index of the power law is $\Gamma = 1.5$. We note that the bottom panel is the residuals between the fit and the data in units of sigma, as chi-squared statistics were used instead of Cash statistics for this system alone.

Table 3. Spectral Fits

IRAS Name	Γ	Temp keV	N_H^{Gal} (cm^{-2}) 10^{20} cm^{-2}
18329+5950 East	$1.5^{+0.5}_{-0.5}$	$0.65^{+0.19}_{-0.17}$	4.48
18329+5950 West	$1.6^{+0.4}_{-0.5}$	$0.69^{+0.25}_{-0.18}$	4.48
19354+4559	$2.4^{+1.1}_{-0.9}$	···	12.0
20550+1656	$1.5^{+0.2}_{-0.1}$	$0.67^{+0.04}_{-0.04}$	11.0

Note. — Comparison of spectral fitting parameters for the two components of IRAS 18329+5950 and the single sources in IRAS 19354+4559 and IRAS 20550+1656. All Galactic column densities are taken from Dickey & Lockman (1990).

4. Discussion

With models in hand, we further investigate the starburst and AGN nature of our sources.

4.1. Comparison to Ranalli et al. 2003

We first compare our measured X-ray luminosities to those predicted by the IR/X-ray relationships presented in Equations (8) and (12) of R03 and reproduced as (2) and (3) below, respectively:

$$\log\left(\frac{L_{0.5-2\ \mathrm{keV}}}{\mathrm{L}_\odot}\right) = \log\left(\frac{L_{\mathrm{FIR}}}{\mathrm{L}_\odot}\right) - 3.68, \tag{2}$$

$$\log\left(\frac{L_{2-10\ \mathrm{keV}}}{\mathrm{L}_\odot}\right) = \log\left(\frac{L_{\mathrm{FIR}}}{\mathrm{L}_\odot}\right) - 3.62,. \tag{3}$$

The FIR luminosity is calculated from the FIR flux, F_{FIR}, which in turn is estimated from the 60 and 100 micron flux densities f_ν, measured in Janskys, by the following relation (Helou et al. 1985):

$$F_{\mathrm{FIR}} = 1.26 \times 10^{-11}[2.58\frac{f_{60\mu\mathrm{m}}}{Jy} + \frac{f_{100\mu\mathrm{m}}}{Jy}]\ \mathrm{W\ m}^2. \tag{4}$$

Since these relationships pertain directly to starbursts and assume negligible AGN contamination, if they hold for our observations we can infer that our systems are most likely dominated by star formation rather than AGN. If AGN activity dominates, however, we would expect an excess in X-ray luminosity compared to these predictions. The 1σ uncertainties on the intercepts that R03 provide for these linear relations are 0.27 and 0.29 for the soft and hard band, respectively.

4.1.1. IRAS 18329+5950

For IRAS 18329+5950, the 60 and 100 micron fluxes reported in the RBGS predict $L_{\mathrm{soft,\ R03}} = 2.0^{+1.7}_{-0.9} \times 10^{41}$ erg s^{-1} and $L_{\mathrm{hard,\ R03}} = 2.3^{+2.2}_{-1.1} \times 10^{41}$ erg s^{-1} from the above R03 linear relations. After accounting for Galactic absorption as in R03, our models find these values to be $L_{\mathrm{soft,\ model}} = 3.9^{+1.9}_{-1.2} \times 10^{40}$ erg s^{-1}, $L_{\mathrm{hard,\ model}} = 3.7^{+1.9}_{-1.0} \times 10^{40}$ erg s^{-1} for 18329E and $L_{\mathrm{soft,\ model}} = 4.2^{+1.5}_{-2.0} \times 10^{40}$ erg s^{-1}, $L_{\mathrm{hard,\ model}} = 4.5^{+0.6}_{-2.0} \times 10^{40}$ erg s^{-1} for 18329W. The system as a whole, then, has an unabsorbed X-ray luminosity of $L_{\mathrm{soft,\ tot}} = 8.1^{+3.3}_{-3.2} \times 10^{40}$ erg s^{-1} and $L_{\mathrm{hard,\ tot}} = 8.2^{+2.4}_{-3.0} \times 10^{40}$ erg s^{-1}. The upper bound of the soft X-ray luminosity is within lower range provided by Equation (2) and the hard X-rays from Equation (3) overpredict our results for the system as a whole.

4.1.2. IRAS 19354+4559

R03 predicts $L_{\rm soft,\,R03} = 9.2^{+8.0}_{-4.2} \times 10^{40}$ erg s^{-1} and $L_{\rm hard,\,R03} = 1.1^{+1.0}_{-0.5} \times 10^{41}$ erg s^{-1} for IRAS 19354+4559. Our model luminosities give $L_{\rm soft,\,model} = 4.5^{+2.0}_{-2.0} \times 10^{40}$ erg s^{-1} and $L_{\rm hard,\,model} = 4.5^{+2.1}_{-1.9} \times 10^{40}$ erg s^{-1}. As with the soft band of IRAS 18329+5950, both the soft and hard bands of IRAS 19354+4559 are on the lower end of the predictions. This should be viewed with caution, however, due to the limitations in this particular spectral model as discussed in §3.2.

4.1.3. IRAS 20550+1656

Using the same method as for both systems above, we see that the RBGS-provided IR data for IRAS 20550+1656 predict $L_{\rm soft,\,R03} = 3.7^{+3.1}_{-1.7} \times 10^{41}$ erg s^{-1} and $L_{\rm hard,\,R03} = 4.2^{+4.0}_{-2.1} \times 10^{41}$ erg s^{-1} after correcting for Galactic absorption. Doing the same, we find luminosities of $L_{\rm soft,\,model} = 1.8^{+0.3}_{-0.2} \times 10^{41}$ erg s^{-1} and $L_{\rm hard,\,model} = 2.9^{+0.5}_{-0.4} \times 10^{41}$ erg s^{-1}. Both of these are on the lower end of the error range of the R03 equations, but are still consistent.

IRAS 20550+1656 was also the subject of an extensive multiwavelength campaign, including an X-ray analysis with *Chandra* that we can compare to our data from *XMM Newton*, as part of the GOALS project (Inami et al. 2010). They were able to distinguish two distinct objects in X-rays (see their Figure 5, labeled as “A” and “C+D”) with Chandra’s spatial resolution, whereas we see only a single source with *XMM Newton*. One of their two X-ray sources was claimed to be extended, covering two distinct IR bright regions seen with *Spitzer*. They report soft X-ray luminosities of $L_{\rm A,\,soft} = 6.6 \times 10^{40}$ erg s^{-1} and $L_{\rm C+D,\,soft} = 1.8 \times 10^{40}$ erg s^{-1}, which, combined, is less than half of the fit value from our model. Their hard X-ray luminosities for the two sources were both $L_{\rm hard} = 10^{41}$ erg s^{-1}, which again sum to below the luminosity that we find. Using their *Spitzer* data on the individual sources, they conclude that source A is most likely a starburst, obeying the R03 relations, whereas for C+D they find that R03 overpredicts the X-ray values for its IR luminosity, as we find for our single source. Their hardness ratio for C+D is 0.05 ± 0.14, but this cannot be compared directly to ours due to the fact that the two instruments have different response functions. For the non-nuclear IR source (labeled “D” in their paper), their highest star formation rate (SFR) prediction is 120 $M_\odot$ yr^{-1}. One possible explanation for the differences in luminosity between the *Chandra* and *XMM* observations is that IRAS 20550+1656 is intrinsically variable, which could be suggestive of an AGN in either source A, source C+D, variations in the extended emission from HMXBs, or combinations thereof. Unfortunately, with the lower spatial resolution of our observation we are unable to determine which of their reported sources, if only one, is responsible for our larger X-ray luminosity.

4.2. Comparison to Symeonidis et al. 2011

Symeonidis et al. (2011), hereafter SY11, examined a larger range in IR luminosities than R03 and found that the R03 relations, while functional for normal IR galaxies (i.e, those with $L_{\rm IR} \leq 10^{11}$ $L_\odot$) tend to overpredict X-ray luminosities for higher IR luminosities such as those in our sample. For higher, LIRG-type IR luminosities, they found (using a modified version of the hard X-ray relation found in Lehmer et al. 2010) the following relationships:

$$\log\left(\frac{L_{0.5\text{–}2\ \mathrm{keV}}}{\mathrm{L}_\odot}\right) = \log\left(\frac{L_{IR}}{\mathrm{L}_\odot}\right) - 4.55, \tag{5}$$

$$\log\left(\frac{L_{2\text{–}10\ \mathrm{keV}}}{\mathrm{L}_\odot}\right) = \log\left(\frac{L_{IR}}{\mathrm{L}_\odot}\right) - 4.38, \tag{6}$$

where the IR luminosity is calculated from the IR flux. This, in turn, is estimated from the IRAS fluxes in the RBGS using the relation

$$F_{\mathrm{IR}} = 1.8 \times 10^{-11}(13.48\frac{f_{12\mu\mathrm{m}}}{Jy} + 5.16\frac{f_{25\mu\mathrm{m}}}{Jy} + 2.58\frac{f_{60\mu\mathrm{m}}}{Jy} + \frac{f_{100\mu\mathrm{m}}}{Jy})\mathrm{W\ m^{-2}\ s^{-1}}. \tag{7}$$

The SY11 relations have a 1σ error of 0.37 in the soft band and a 2σ error of 0.68 in the hard band.

Because our systems are only marginally within the luminosity range spanned by the galaxies used to create the R03 relationships, we also compare our model values to SY11. For IRAS 18329+5950, its RBGS IR fluxes predict X-ray components of $L_{\text{soft, SY11}} = 4.8^{+6.5}_{-2.8} \times 10^{40}$ erg s^{-1} and $L_{\text{hard, SY11}} = 7.2^{+21}_{-5.7} \times 10^{40}$ erg s^{-1}. Our soft value is within the upper error bounds, and our hard value is consistent with this prediction. In the case of IRAS 20550+1656, Equations (5) and (6) give $L_{\text{soft, SY11}} = 9.4^{+18}_{-5.4} \times 10^{40}$ erg s^{-1} and $L_{\text{hard, SY11}} = 1.4^{+5.3}_{-1.1} \times 10^{41}$ erg s^{-1}. Our values are above both of these, but well within the errors of the soft and hard band relations.

Noting that a lack of counts forced us to use an overly simplified model for IRAS 19354+4559, we cautiously investigate how our data on this system compares to values derived from the SY11 relations. The flux upper limits from the RBGS predict $L_{\text{soft, SY11}} = 7.7^{+10}_{-4.3} \times 10^{40}$ erg s^{-1} and $L_{\text{hard, SY11}} = 1.4^{+6.6}_{-0.9} \times 10^{41}$ erg s^{-1}. Our soft and hard band luminosities are lower than these predictions, but within the provided SY11 uncertainties, which is shown Figure 7.

4.3. Summary of X-ray/IR Relations

In our systems, the measured IR and X-ray luminosities are consistent to within 2σ of the empirical relation in SY11, which is appropriate for higher-IR luminosity galaxies. The R03 relations slightly overpredict the X-ray luminosity, which may arise from the fact that they were derived using lower-IR luminosity systems. The discrepancy with R03 is, however, lower than 1.5σ on each individual object. We suggest that future work, when attempting to extrapolate an X-ray luminosity from IR values for star formation, use the SY11 relations when looking in the LIRG regime.

Could something unique be happening in this luminosity space? Iwasawa et al. (2011) analyzed the X-ray properties of a subsample of GOALS objects using *Chandra* and argued that there was a distinct change in the hard X-ray luminosity for objects in the range $\log(L_{\mathrm{IR}}/\mathrm{L}_\odot) = 11.0$–$11.73$. They concluded that HMXBs fade in relevance as the dominating X-ray source for the especially IR-bright systems. What replaces them is uncertain, but it is possible that AGN activity, which is not being traced by either R03 or SY11, becomes a noticeable contributor in this regime in some systems.

4.4. Star Formation Rates

With known X-ray and IR luminosities, we now investigate the star formation rates in these systems. As there are multiple relations available in the literature, we compare several different values. Using the X-ray star formation equations from R03,

$$\begin{aligned} \mathrm{SFR}(\mathrm{M}_\odot\ \mathrm{yr}^{-1}) &= 2.2 \times 10^{-40} L_{0.5-2\ \mathrm{keV}} \text{ and} && (8) \\ &= 2.0 \times 10^{-40} L_{2-10\ \mathrm{keV}}, && (9) \end{aligned}$$

the apparent SFR of IRAS 18329+5950 as a whole, using our model luminosities, is 18 and 16 $\mathrm{M}_\odot$ yr^{-1} based on the soft and hard X-ray bands, respectively. As described in §1, these relations supposedly measure the X-ray luminosities from XRBs that are born during episodes of star formation, thus tracing the SFR. R03 calibrate Equations 8 and 9 using the Kennicutt (1998) IR starburst relations given by

$$\mathrm{SFR}(\mathrm{M}_\odot\ \mathrm{yr}^{-1}) = \frac{1}{5.8 \times 10^9} \frac{L_{\mathrm{FIR}}}{\mathrm{L}_\odot}. \qquad (10)$$

From 10, we find star formation rates 42 $\mathrm{M}_\odot$ yr^{-1}. These values are in the regime of starburst galaxies, though they span a range of almost a factor of three between R03 and Kennicutt (1998).

Using the X-ray/SFR relations provided in Equations 8 and 9 for our X-ray luminosities for IRAS 19354+4559, we find star formation rates of 10 $\mathrm{M}_\odot$ yr^{-1} and 9 $\mathrm{M}_\odot$ yr^{-1}, respectively.

The observed soft (hard) X-ray luminosity of IRAS 20550+1656 gives a star formation rate of 40 (59) $\mathrm{M}_\odot$ yr^{-1}, while Equation (10) gives a value 79 $\mathrm{M}_\odot$ yr^{-1}.

There is an appreciable spread in the range of these star formation rates, but the values imply that at least one of the galaxies in each of the systems is a starburst. The R03 values in all of our sources are rather close to that from Kennicutt (1998), as would be expected based on the fact that R03 used them to calibrate their own relations. The inconsistency in these values, where the star formation rate derived from X-ray luminosities is less than those derived from IR luminosities, is also in the direction of what has been noted already. Our systems are X-ray faint for their IR luminosities in the standard R03 relations, so it is not too surprising that the R03 SFRs, which use their own X-ray/IR luminosity scaling, give larger rates for our systems which fell below their best fit. The Kennicutt relations also have a systematic uncertainty of about 30% (Kennicutt 1998). It is plausible that the combination of these two factors can account for some of the discrepancy in the two sets of rates.

The underlying assumption in most of these relations is that all of the UV emission is from O and B stars, whose presence is indicative of recent star formation, and this emission is reprocessed by dust into the infrared. This is not necessarily the case, however, and Miralles-Caballero (2012) observed some star

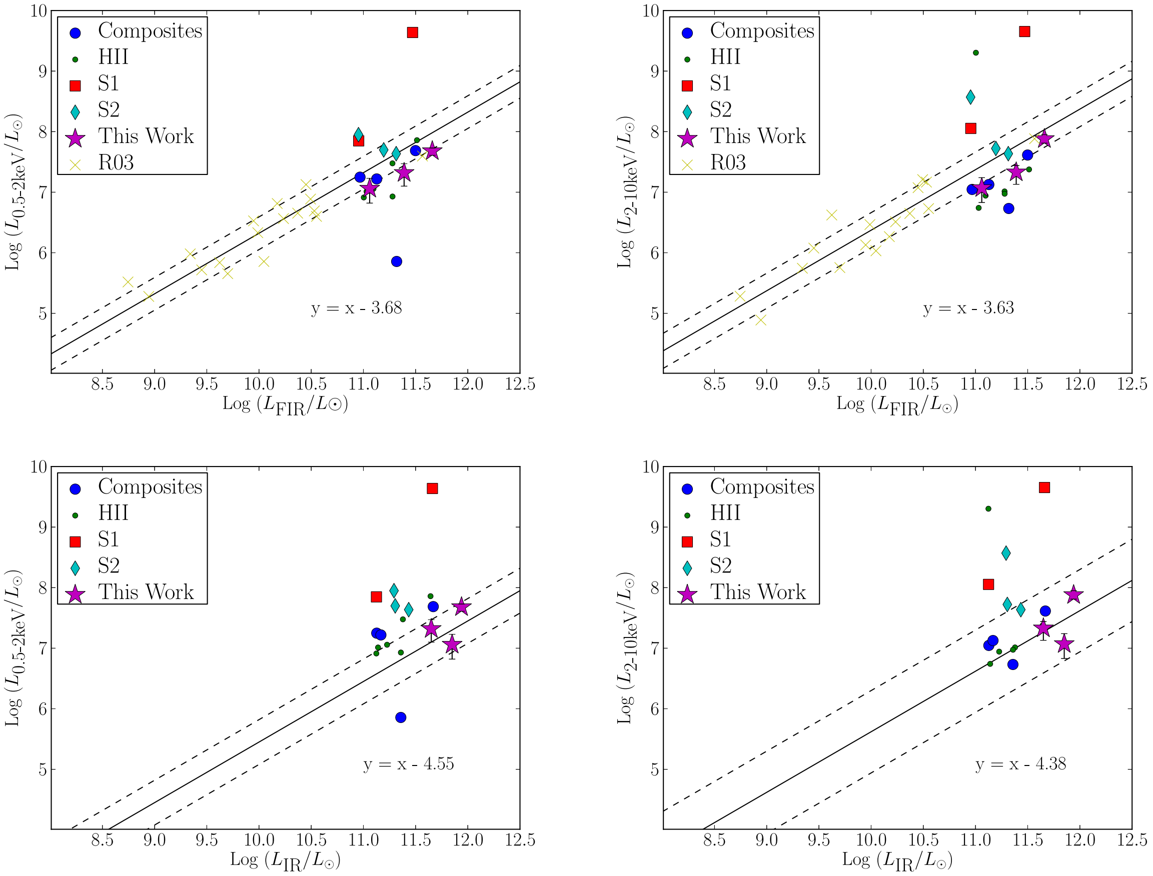

Fig. 7.— Comparison between the modeled X-ray luminosities of our three systems with predictions from IR/X-ray luminosity relations. *Top*: Plots of the R03 soft band (*left*, Equation 2) and hard band (*right* Equation 3) relationships. Crosses represent data from R03 best fit by the solid line and 1σ errors with dot-dash lines. Stars represent our data, notably in a region where their data is much scarcer. *Bottom*: Plots of the SY11 soft (*left*, Equation 5) and hard (*right*, Equation 6) IR/X-ray relationships, with dot-dash lines being the one and two sigma errors for the soft and hard bands, respectively. Note that here our soft data are on the lower bounds of R03 and upper bounds for SY11, but within error tolerances for all four cases. The extra data points were compiled by Pereira-Santaella et al. (2011), and taken from Lehmer et al. (2010) for NGC 23, NGC 5653, and Zw049.057, Miniutti et al. (2007) for MCG-03-34-064, Levenson et al. (2005) for NGC 7130, and Blustin et al. (2003) for NGC 7469. Our systems tend to lie in a region occupied by HII and composite AGN/starbursts.

clusters with as much as 15% unobscured UV radiation. This finding implies that our values, which do not take into account any escaping UV flux, are only lower bounds on the total star formation rate. Given our large uncertainties, however, this may be a negligible contributing factor.

4.5. AGN in LIRGs?

We have employed several methods to determine whether or not our sample contains AGN or dual AGN. One indicator would be X-ray point sources. From Figure 1 we see that all three systems are detected in the entire XMM energy bandpass and that IRAS 18329+5950 is composed of two distinct sources. If these X-ray sources were due solely to the presence of an AGN, one would expect that their radial profiles would be similar to the detector's PSF. From Figure 2 we see that, for the most part, the 2-8 keV emission is more extended than the model 5 keV PSF. It is impossible to say from this alone, however, whether AGN or other separate objects, such as LMXBs/HMXBs, are the culprits because the presence of a starburst could blur out any point-like AGN emission or large column depths could obscure strong sources.

The second test was to compare the spectra of each system to starburst and AGN templates. Both sources in IRAS 18329+5950 and the single source in IRAS 20550+1656 were composed of a MEKAL plasma, typically associated with ionizing photons from OB stars and their supernovae, and a power law, which could be from either an AGN or X-ray binaries. As for their spectral indices, X-ray binaries are expected, from Persic & Rephaeli (2002), to have power law slopes of $\sim$1.2, though values in the literature range from 1–3. The power law components of IRAS 18329+5950 as well as IRAS 20550+1656 are on the upper end of this range. IRAS 19354+4559 is steeper but consistent within its error bars. If it is truly greater than 2, this could be due to the limitations in model complexity from low counts, the presence of a low luminosity AGN, or both.

Lastly, we compared our X-ray values to predictions from two separate IR/X-ray relationships derived from star formation. The first set, from R03, was taken from a sample of lower-IR-luminosity galaxies filtered for AGN contamination. All of our systems' X-ray luminosities lie near or below the lower limit of what their IR fluxes from the RBGS would predict from star formation alone. We then examine the SY11 relationships, which are argued to be more applicable for IR luminosities above $10^{11}L_{\odot}$, the regime of our systems, and discover that our model luminosities are mostly well fit or on the higher end of expectations from star formation alone on this scale.

In all of these tests, we do not find robust evidence for AGN activity in any of our sources, though we cannot definitively rule out AGN activity either.

This, then, begs the question of why there are no dual AGN, or even single AGN, signatures in our systems. The most likely explanation is a lack of imaging and spectral data, especially the latter. Currently, our systems lie primarily between the R03 and SY11 predictions, but IRAS 18329+5950 and IRAS 19354+4559 have large uncertainties in their luminosities. Better data would allow us to determine with more certainty whether or not these systems are consistent with either relation. It would also permit us to attempt to fit more complex models with higher constraining power. This is a severe problem with IRAS 19354+4559 in particular, as we could only fit it with a single power law component which clearly has a soft excess, as shown in Figure 5. The biggest obstacle among all our systems was perhaps the loss of large portions of our exposures due to flaring, particularly in IRAS 18329+5950 and IRAS 19354+4559. Additionally, the enhanced spatial resolution of Chandra might be able to discern two distinct nuclear sources, as in the case of IRAS 20550+1656 in Inami et al. (2010).

It is also possible that any AGN present in our systems is Compton thick with large ($> 10^{24}$ cm^{-2}) column densities, hiding nuclear activity. Knowing that these systems are heavily obscured in the optical, we investigated the location of our systems on a BPT diagram (Baldwin et al. 1981) of N[II]/Hα against O[III]/Hβ. In Figure 8 we show IRAS 18329+5950 and IRAS 20550+1656 (Hβ: Kennicutt et al. 2009, [NII], [OIII], and Hα: Moustakas & Kennicutt 2006) alongside data and classifications taken from Veilleux & Osterbrock (1987) as reference, and see that they lie in the same region as the starbursts (SBs) and narrow emission line galaxies (NELGs, those galaxies with profiles akin to HII and LINER systems), similar to Figure 7. We also looked for mid-IR lines in the literature that would be less subject to internal extinction than the optical ones. Only one was encountered (Inami et al. 2010), which suggested the system was a starburst rather than an AGN.

Our data is also consistent with there being no AGN present at all. What does this imply? It could be that there is a problem in the merger scenario presented in §1 on the major assembly and activation of most SMBHs by galaxy-galaxy interactions. Given the small number of systems reported with dual AGN and the larger number of attempts to find them through varied methods, there could also be an issue with this phase of the hierarchical growth route altogether. Some fraction, possibly substantial, of SMBHs may not accrete much material during mergers, in which case one might expect most of the AGN activity to occur during slower secular accretion processes. If that were indeed the case, then finding binary AGN in mergers would be quite difficult. Alternatively, perhaps intense star formation due to the merger process is able to consume most of the potential AGN fuel before it reaches the orbiting SMBHs and ignites them. The star formation processes also are quite powerful in mergers, and can possibly dwarf lower luminosity AGN activity that occurs as the SMBHs begin to accrete matter. Or, maybe the lifetime of dual AGN activity is extremely short and thus hard to observe, as some simulations (Van Wassenhove et al. 2012) have suggested. It could be that one of our assumptions in creating our sample selection criteria is incorrect as well. For instance, Class III mergers, contrary to our initial hypothesis, may be too early in the merger process to have AGN activity in the systems. Unfortunately, our data cannot discriminate between these scenarios and we are unable to definitively state which, if any, is the true culprit at this time.

5. Conclusion

We present the results from a search for dual AGN. Based on the environment arguments presented in §1, we selected for nearby LIRGs (tending to have lower L_{IR} than those observed at higher redshifts) with galaxy separations near the resolution limit of the *XMM Newton* and with evidence of interaction. The only system in which two distinct X-ray sources are resolved is IRAS 18329+5950.

Table 4. IR and X-ray Luminosities

IRAS Name	$L_{\rm FIR}$ $\log(L_{\rm FIR}/{\rm L}_\odot)$	$L_{\rm IR}$ $\log(L_{\rm IR}/{\rm L}_\odot)$	R03$_{\rm soft}$ $\log(L_{\rm soft}/{\rm L}_\odot)$	SY11$_{\rm soft}$ $\log(L_{\rm hard}/{\rm L}_\odot)$	R03$_{\rm hard}$ $\log(L_{\rm soft}/{\rm L}_\odot)$	SY11$_{\rm hard}$ $\log(L_{\rm hard}/{\rm L}_\odot)$
18329+5950	11.39	11.65	7.71 ± 0.27	7.10 ± 0.37	7.77 ± 0.29	7.27 ± 0.68
19354+4559	11.06	11.85	7.38 ± 0.27	7.30 ± 0.37	7.44 ± 0.29	7.47 ± 0.68
20550+1656	11.66	11.94	7.98 ± 0.27	7.39 ± 0.37	8.04 ± 0.29	7.56 ± 0.68

Note. — Predicted X-ray luminosities based on IR and FIR luminosity relations. All IR luminosities are calculated from the fluxes presented in the RBGS (Sanders et al. 2003). Here and throughout the paper, the soft band is 0.5–2 keV and the hard band is 2–10 keV. Also note that the errors on SY11$_{\rm hard}$ are 2σ whereas the rest are 1σ, or approximately so in the case of R03 (Ranalli et al. 2003).

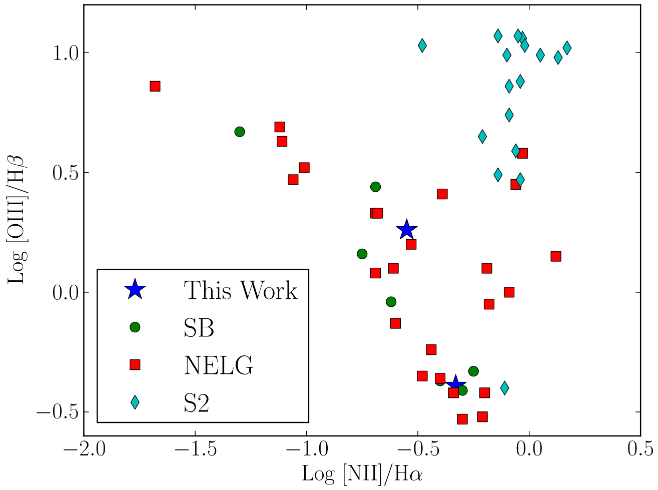

Fig. 8.— BPT diagram from Veilleux & Osterbrock (1987) with IRAS 18329+5950 and IRAS 20550+1656 added. They occupy the same parameter space as narrow emission line galaxies and starburst systems.

If we take the predicted starburst-originating X-ray values from Ranalli et al. (2003), the best fit models for IRAS 18329+5950, IRAS 19354+4559, and IRAS 20550+1656 are all somewhat underluminous in X-rays if we, as they did, do not correct for intrinsic absorption. Given our systems' uncertainties, however, they mostly remain within 1σ of the predicted value for both the soft and hard bands. If we use the relations presented in Symeonidis et al. (2011) for star-formation/X-ray instead, reproduced here as (5) and (6), however, we find that our models are well fit, or even slightly overluminous in X-rays for a star formation origin, though within 2σ of the relations they provided.

Under these circumstances, an optimistic interpretation of IRAS 18329+5950 would categorize it as a dual AGN candidate with hybrid starburst activity, since two separate objects are seen at the correct distances from one another to indicate heightened nuclear activity. The data for each of our systems, however, is not of sufficient quality to find or conclusively rule out the presence of AGN. Regardless of the dual AGN status of our systems, the luminosities here may provide some additional support for the implications found in Iwasawa et al. (2011) and SY11, namely that there appears to be a characteristic change in X-ray behavior, and thus possibly a change in the sources of X-rays, in the regime of lower luminosity LIRGs, as well as a diminishing effect from star bursting as predicted by R03. These results could be improved upon by searching for other nearby LIRG systems with resolvable nuclear regions. If they continue, as the systems presented in this paper, to be deficient in expected X-ray luminosity, then we will either need to rethink our IR/X-ray relationships based on star formation in this regime or quantify the contribution from AGN contamination.

We would like to thank the XMM Science Team for their invaluable advice with data processing and useful assistance. We are also extremely grateful to Scott Adams, Joe Antognini, Ben Shappee, Garrett Somers, and Obright Lorain for help along the way.

REFERENCES

Ajello, M., Alexander, D. M., Greiner, J., Madejski, G. M., Gehrels, N., & Burlon, D. 2012, arXiv:astro-ph/1202.3137

Alonso-Herrero, A., Pereira-Santaella, M., Rieke, G. H., & Rigopoulou, D. 2011, arXiv:astro-ph/1109.1372

Anders, E., & Grevesse, N. 1989, Geochim. Cosmochim. Acta, 53, 197

Armus, L., et al. 2009, PASP, 121, 559

Arribas, S., Bushouse, H., Lucas, R. A., Colina, L., & Borne, K. D. 2004, AJ, 127, 2522

Baan, W. A., Salzer, J. J., & Lewinter, R. D. 1998, ApJ, 509, 633

Baldwin, J. A., Phillips, M. M., & Terlevich, R. 1981, PASP, 93, 5

Bauer, F. E., Alexander, D. M., Brandt, W. N., Schneider, D. P., Treister, E., Hornschemeier, A. E., & Garmire, G. P. 2004, AJ, 128, 2048

Bell, E. F., et al. 2011, arXiv:astro-ph/1110.3786

Blustin, A. J., et al. 2003, A&A, 403, 481

Braito, V., Reeves, J. N., Della Ceca, R., Ptak, A., Risaliti, G., & Yaqoob, T. 2009, A&A, 504, 53

Cash, W. 1979, ApJ, 228, 939

Charmandaris, V., Wu, Y., Huang, J., Spinoglio, L., & Tommasin, S. 2010, in IAU Symposium, Vol. 267, IAU Symposium, 254–259

Dickey, J. M., & Lockman, F. J. 1990, ARA&A, 28, 215

Draper, A. R., & Ballantyne, D. R. 2012, ApJ, 751, 72

Ellison, S. L., Patton, D. R., Mendel, J. T., & Scudder, J. M. 2011, MNRAS, 418, 2043

Fabbiano, G. 2006, ARA&A, 44, 323

Fabian, A. C. 1999, MNRAS, 308, L39

Fiore, F., et al. 2000, New A, 5, 143

Georgakakis, A., et al. 2011, MNRAS, 418, 2590

Haardt, F., & Maraschi, L. 1993, ApJ, 413, 507

Helou, G., Soifer, B. T., & Rowan-Robinson, M. 1985, ApJ, 298, L7

Hopkins, P. F., Hernquist, L., Cox, T. J., Di Matteo, T., Robertson, B., & Springel, V. 2006, ApJS, 163, 1

Inami, H., et al. 2010, AJ, 140, 63

Iwasawa, K., et al. 2011, A&A, 529, A106

Kennicutt, Jr., R. C. 1998, ApJ, 498, 541

Kennicutt, Jr., R. C., et al. 2009, ApJ, 703, 1672

Komossa, S. 2006, Mem. Soc. Astron. Italiana, 77, 733

Komossa, S., Burwitz, V., Hasinger, G., Predehl, P., Kaastra, J. S., & Ikebe, Y. 2003, ApJ, 582, L15

Koss, M., Mushotzky, R., Veilleux, S., Winter, L. M., Baumgartner, W., Tueller, J., Gehrels, N., & Valencic, L. 2011, ApJ, 739, 57

Lawrence, A., et al. 1999, MNRAS, 308, 897

Lehmer, B. D., Alexander, D. M., Bauer, F. E., Brandt, W. N., Goulding, A. D., Jenkins, L. P., Ptak, A., & Roberts, T. P. 2010, ApJ, 724, 559

Levenson, N. A., Weaver, K. A., Heckman, T. M., Awaki, H., & Terashima, Y. 2005, ApJ, 618, 167

Liedahl, D. A., Osterheld, A. L., & Goldstein, W. H. 1995, ApJ, 438, L115

Mewe, R., Gronenschild, E. H. B. M., & van den Oord, G. H. J. 1985, A&AS, 62, 197

Mewe, R., Lemen, J. R., & van den Oord, G. H. J. 1986, A&AS, 65, 511

Miniutti, G., Ponti, G., Dadina, M., Cappi, M., & Malaguti, G. 2007, MNRAS, 375, 227

Miralles-Caballero, D. 2012, arXiv:astro-ph/1202.5179

Moustakas, J., & Kennicutt, Jr., R. C. 2006, ApJS, 164, 81

Muzzin, A., et al. 2012, ApJ, 746, 188

Pereira-Santaella, M., et al. 2011, A&A, 535, A93

Persic, M., & Rephaeli, Y. 2002, A&A, 382, 843

—. 2003, A&A, 399, 9

Piconcelli, E., et al. 2010, ApJ, 722, L147

Ptak, A., Heckman, T., Levenson, N. A., Weaver, K., & Strickland, D. 2003, ApJ, 592, 782

Ranalli, P., Comastri, A., & Setti, G. 2003, A&A, 399, 39

Sanders, D. B., Mazzarella, J. M., Kim, D.-C., Surace, J. A., & Soifer, B. T. 2003, AJ, 126, 1607

Sanders, D. B., & Mirabel, I. F. 1996, ARA&A, 34, 749

Sani, E., Lutz, D., Risaliti, G., Netzer, H., Gallo, L. C., Trakhtenbrot, B., Sturm, E., & Boller, T. 2010, MNRAS, 403, 1246

Santini, P., et al. 2012, arXiv:astro-ph/1201.4394

Serber, W., Bahcall, N., Ménard, B., & Richards, G. 2006, ApJ, 643, 68

Shapiro, S. L., Lightman, A. P., & Eardley, D. M. 1976, ApJ, 204, 187

Summers, L. K., Stevens, I. R., Strickland, D. K., & Heckman, T. M. 2004, MNRAS, 351, 1

Sunyaev, R. A., & Titarchuk, L. G. 1980, A&A, 86, 121

Surace, J. A. 1998, PhD thesis, Institute for Astronomy University of Hawaii 2680 Woodlawn Dr. Honolulu, HI 96822

Symeonidis, M., et al. 2011, MNRAS, 417, 2239

Teng, S. H., et al. 2009, ApJ, 691, 261

Tombesi, F., Cappi, M., Reeves, J. N., Palumbo, G. G. C., Yaqoob, T., Braito, V., & Dadina, M. 2010, A&A, 521, A57

Toomre, A., & Toomre, J. 1972, ApJ, 178, 623

Van Wassenhove, S., Volonteri, M., Mayer, L., Dotti, M., Bellovary, J., & Callegari, S. 2012, ApJ, 748, L7

Vattakunnel, S., et al. 2011, arXiv:astro-ph/1111.3285

Veilleux, S., Kim, D.-C., & Sanders, D. B. 2002, ApJS, 143, 315

Veilleux, S., & Osterbrock, D. E. 1987, ApJS, 63, 295

Wilms, J., Allen, A., & McCray, R. 2000, ApJ, 542, 914

Yuan, T.-T., Kewley, L. J., & Sanders, D. B. 2010, ApJ, 709, 884

This preprint was prepared with the AAS LaTeX macros v5.2.